nanomaterials

MDPI

Article

Synthesis and Characterization of Zinc and Vanadium Co-Substituted $CoFe_2O_4$ Nanoparticles Synthesized by Using the Sol-Gel Auto-Combustion Method

Parvin Imanipour [1], Saeed Hasani [1,*], Amir Seifoddini [1] and Marcin Nabiałek [2]

[1] Department of Mining and Metallurgical Engineering, Yazd University, Yazd 89195-741, Iran; elmira.ip7070@gmail.com (P.I.); seifoddini@yazd.ac.ir (A.S.)
[2] Department of Physics, Częstochowa University of Technology, 42-200 Częstochowa, Poland; marcin.nabialek@pcz.pl
* Correspondence: hasani@yazd.ac.ir; Tel.: +98-3531232601; Fax: +98-3538210995

Abstract: In recent years, cobalt ferrite has attracted considerable attention due to its unique physical properties. The present study aimed to produce cobalt ferrite magnetic nanoparticles doped with zinc and vanadium using the sol-gel auto-combustion method. For this purpose, $Co_{1-x}Zn_xFe_{2-y}V_yO_4$ (where x = 0.0, 0.1, 0.2, 0.5 and y = 0.00, 0.05, 0.15, 0.25) precursors were calcined at 800 °C for 3 h. The prepared samples were characterized with the X-ray diffraction (XRD) method in combination with Rietveld structure refinement, field emission scanning electron microscopy (FE-SEM), Fourier transform infrared spectroscopy (FT-IR), and vibrating sample magnetometery (VSM). The XRD patterns confirmed the formation of crystalline spinel structure for all samples. However, the diffraction peaks of hematite and iron vanadium oxide phases were observed in the patterns of some doped samples. The average crystallite size for all the synthesized samples was found to be in the range of ~45–24 nm, implying that it decreased by simultaneously doping cobalt ferrite with Zn and V. The FT-IR spectrum confirmed the formation of the spinal structure of ferrite through the observed vibrational bands assigned to the tetrahedral (υ_2) and octahedral (υ_1) interstitial complexes in the spinel structure. The FE-SEM images showed that morphology, average grain size, and agglomeration of the synthesized powders were affected by doping, which was due to the interactions of the magnetic surface of nanoparticles. The VSM curves demonstrated that saturation magnetization and coercivity values changed in the range of 30–83 emu/g and from 27–913 Oe, respectively. These changes occurred due to the alteration in cation distribution in the spinel structure. This can be attributed to the change in superexchange interactions between magnetic ions by co-substitution of Zn and V ions in Cobalt ferrite and the changes in magnetocrystalline anisotropy.

Keywords: cobalt ferrite; doping elements; magnetic properties; coercivity; sol-gel method

Citation: Imanipour, P.; Hasani, S.; Seifoddini, A.; Nabiałek, M. Synthesis and Characterization of Zinc and Vanadium Co-Substituted $CoFe_2O_4$ Nanoparticles Synthesized by Using the Sol-Gel Auto-Combustion Method. *Nanomaterials* **2022**, *12*, 752. https://doi.org/10.3390/nano12050752

Academic Editor: Eva Pellicer

Received: 31 January 2022
Accepted: 18 February 2022
Published: 23 February 2022

1. Introduction

In recent decades, the synthesis of nanostructured spinel ferrites with the general formula MFe_2O_4 (where M = Co, Ni, Mg, Mn, etc.) has been investigated in order to improve their unique properties such as magneto-optical properties [1–3], catalytic properties [4,5], electrical resistivity [6], magneto-resistivity [7], biocompatibility [8–10], porosity [11], etc. The spinel ferrites have a cubic unit cell containing 56 atoms, where 32 of them are oxygen anions, and the other 24 atoms are metallic cations of which only eight occupy tetrahedral sites (A-site) while the other 16 atoms occupy octahedral sites (B-site) [12,13]. Among spinel ferrite nanoparticles, pure cobalt ferrite and its substituted compounds have attracted the considerable attention of numerous researchers in recent decades due to the reliable saturation magnetization (M_s) [14], moderate magnetocrystalline anisotropy (K) [15,16], high coercivity (H_c) [17], high Curie temperature (T_c) [18], and thermal stability [19,20]. It is accepted that the chemical, electrical, and magnetic properties of cobalt ferrite nanoparticles

are dependent on the chemical composition, cation distribution in the two sub-lattices of A- and B-sites, morphology, surface properties, and preparation method [21–24]. For instance, these nanoparticles are often synthesized by various routes such as co-precipitation [25,26], ultrasound irradiation, solution combustion [27], solid-state reaction [28], the conventional ceramic method [29], ball milling [30], and sol-gel auto combustion [31] methods. Among these methods, the sol-gel method is known as a suitable technique to produce nanoparticles with high homogeneity, proper microstructure, and other suitable properties [32–34].

On the other hand, cation distribution in the nanoparticles controls their magnetic behavior, so that these nanoparticles can show a ferromagnetic, super-paramagnetic, or antiferromagnetic behavior [6,35–37]. Therefore, the addition or doping of other elements instead of the Fe- and/or Co- sites has been the subject of much research [38–41]. It is reported that Zn [42–44] and V [43,45] can strongly affect the structural and physical properties of cobalt ferrite. Substitution of Zn^{2+} ion on the Fe- or/and Co- site in cobalt ferrite considerably was reported [27,42,46,47]. For instance, Kumar et al. [41] studied the substitution of Zn^{2+} at the Fe site of $CoZn_xFe_{2-x}O_4$ nanoparticles and found that the saturation magnetization and magnetocrystalline anisotropy are increased for $x \geq 0.15$, but the coercivity is decreased by adding Zn^{2+}. On the other hand, the effect of vanadium doping on the magnetic properties of cobalt ferrite has been investigated [43,45]. The obtained results showed that the V-doped cobalt ferrite indicates a higher coercivity than the pure cobalt ferrite. Therefore, Zn and V, as two doping elements, have the opposite effect on the magnetic properties of these nanoparticles. In this regard, adding more than one element is known as one of the most effective methods to modify the structural and magnetic properties of these nanoparticles [48–50]. Therefore, in the present study, co-substitution of Zn and V at Co and Fe sites, respectively, and their effects on the structural and magnetic properties of $CoFe_2O_4$ nanoparticles were investigated.

2. Materials and Methods

2.1. Materials

Merck Company supplied all of the materials used in this work with analytic grade reagents. The chemical reagents were Cobalt (II) nitrate hexahydrate ($Co(NO_3)_2{\cdot}6H_2O$, ≥99%), iron (III) nitrate nonahydrate ($Fe(NO_3)_3{\cdot}9H_2O$, ≥99%), Zinc nitrate tetrahydrate ($Zn(NO_3)_2{\cdot}4H_2O$, ≥99%), ammonium monovanadate (NH_4VO_3, ≥99%), citric acid (≥99.5%), and ammonia solution (≥25%). Additionally, double-distilled water (DDW) was used as the solvent.

2.2. Samples Preparation

$Co_{1-x}Zn_xFe_{2-y}V_yO_4$ (where x = 0.0, 0.1, 0.2, 0.5 and y = 0.00, 0.05, 0.15, 0.25) nanopowders were synthesized via the sol-gel auto combustion method. The chemical composition of these specimens is presented in Table 1. The stoichiometric amounts of nitrate precursors along with citric acid were weighted as 1:2 ratios and were dissolved in DDW using a magnetic stirrer. Then, ammonia solution is added dropwise to maintain the pH at ~6. By adding a small amount of ammonia solution, a slight increase in the turbidity of the solution was observed. After that, the precursor's mixture was continuously stirred at 80 °C for 3 h until the puffy dark brown gel appeared. With an increase in temperature up to 300 °C, the viscous gel began to froth, and a dried gel achieves. Then, a brownish-black powder was observed. Finally, the prepared powder was sintered at 800 °C for 3 h to obtain crystalline cobalt ferrite nanoparticles. To further clarify the production process, a schematic diagram representing the synthesis process is shown in Figure 1.

Table 1. Chemical composition of the synthesized samples.

Sample Code	Chemical Composition
A	$CoFe_2O_4$
B	$Co_{0.5}Zn_{0.5}Fe_2O_4$
C	$CoFe_{1.75}V_{0.25}O_4$
D	$Co_{0.9}Zn_{0.1}Fe_{1.95}V_{0.05}O_4$
E	$Co_{0.9}Zn_{0.1}Fe_{1.90}V_{0.15}O_4$
F	$Co_{0.9}Zn_{0.1}Fe_{1.75}V_{0.25}O_4$
G	$Co_{0.8}Zn_{0.2}Fe_{1.95}V_{0.05}O_4$
H	$Co_{0.8}Zn_{0.2}Fe_{1.85}V_{0.15}O_4$
I	$Co_{0.8}Zn_{0.2}Fe_{1.75}V_{0.25}O_4$
J	$Co_{0.5}Zn_{0.5}Fe_{1.95}V_{0.05}O_4$
K	$Co_{0.5}Zn_{0.5}Fe_{1.85}V_{0.15}O_4$
L	$Co_{0.5}Zn_{0.5}Fe_{1.75}V_{0.25}O_4$

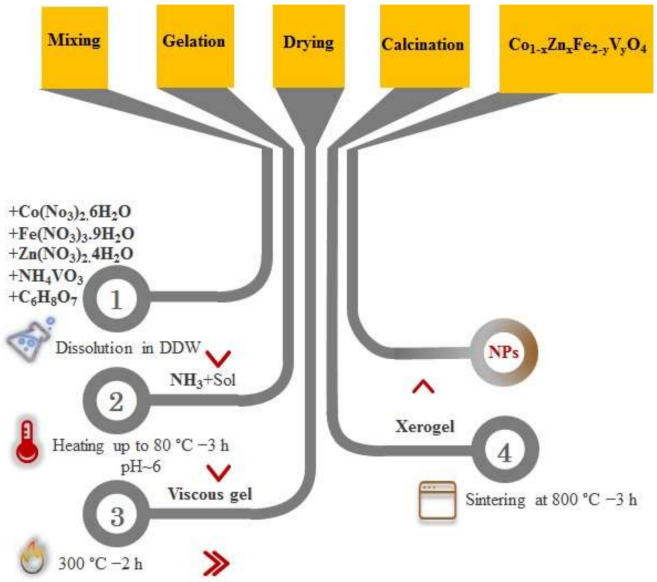

Figure 1. A schematic diagram representing the synthesis process used in the present study.

2.3. Characterization Technique

Determination of phase purity and their identification was done with the X-ray diffraction (XRD) method using a Philips powder diffractometer PW1730 with Cu kα radiation. All of the samples were tested in continuous mode from 20 to 70°. The constitutional analysis in a more accurate profile of all the samples was studied by Rietveld refinements that was performed using PANalytical X'Pert HighScore Plus software (version: 3.0e (3.0.5)). The size and morphology of the samples were analyzed using field emission scanning electron microscopy (FE-SEM; MIRA 3 Tescan, Kohoutovice, Czech Republic.). The thermal behavior of the xerogels was investigated by the non-isothermal differential thermal analysis-thermogravimetry (DTA-TG; Bahr 503, Hüllhorst, Germany), at a heating rate of 20 °C/min up to 1200 °C under air atmosphere. The Fourier transformed infrared (FT-IR; Avatar, Thermo, Waltham, USA) spectra of the samples A, F, and K were recorded in the range 400–4000 cm^{-1}. Moreover, magnetization measurements were carried out using a vibration sample magnetometery (VSM; Magnetic Daghigh Daneshpajouh, Kashan, Iran) at room temperature.

3. Results

3.1. Thermal Behavior

The thermal behavior of the xerogels is investigated using the non-isothermal DTA-TG analyses. For instance, the DTA-TG curves of xerogels related to the samples A, B, and K are presented in Figure 2. This figure illustrates the evolution of TG (shown as dashed lines) and DTA curves. It is obvious that the evaporation of water molecules, decomposition process, and formation of spinel ferrite could be completed below 800 °C, which is in agreement with reported by literature [43,47]. Additionally, the DTA curves show obviously three exothermic peaks in the range of (i) ~RT–292, (ii) ~310–552, and (iii) ~556–1000 °C. The temperature characteristics of these peaks, along with the weight loss percentage, are presented in Table 2. It is notable that the first and second DTA peaks overlap each other, but are well separated from the third DTA peak. The first exothermic peak is mainly due to the combustion of some volatiles. Of course, evaporation of the structural water also occurs in this temperature range, which can be effective for the weight loss observed in this stage. However, the result of these reactions occurring in this temperature range is observed, as an exothermic step.

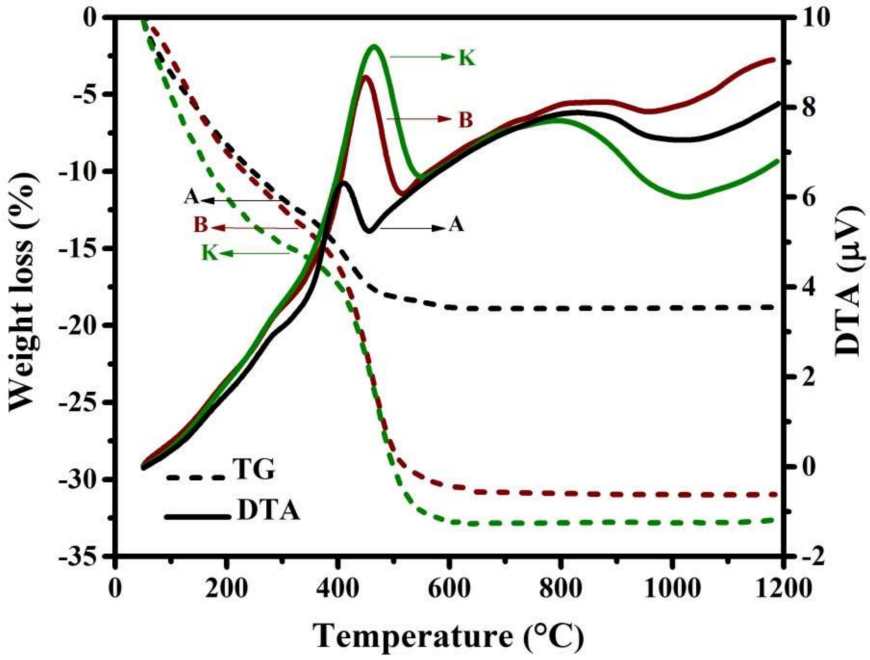

Figure 2. DTA-TG curves related to the samples A, B, and K at a heating rate of 20 °C/min.

Table 2. The DTA peak temperatures and mass loss occurred in every stage, extracted from DTA-TG curves (presented in Figure 2).

Samples	DTA Peak Temp. (°C)			TG-Mass Loss (%)	
	i	ii	iii	i	ii
A	277.8	409.8	826.2	13.1	17.6
B	282.0	450.1	852.5	15.6	28.8
K	292.0	463.9	792.6	16.4	31.6

The second exothermic peak and corresponding TG profile are related to the decomposition of the nitrate salts and other organic compounds, as well as the formation of the spinel ferrite. However, it can be observed that this exothermic peak becomes higher and broader with co-substitution of Zn and V at Co and Fe sites, respectively, which can be due to an increase in the formation enthalpy. In addition, the weight loss at this stage increases by doping.

Moreover, the third exothermic DTA peak (as a broad peak) referred to the powder densification, as mentioned in the literature [47], and therefore no noticeable weight loss is observed at this stage.

3.2. X-ray Diffraction and Structural Studies

The XRD patterns of all samples are presented in Figure 3. As seen, there are several typical diffraction characteristic peaks related to the cubic spinel structures, which is assigned to (220), (311), (222), (400), (422), (511), and (440) planes (JCPDS reference card #96-591-0064). However, by co-substitution of Zn and V at Co and Fe sites, respectively, the diffraction peaks of hematite (Fe_2O_3, JCPDS reference card #96-591-0083) and iron vanadium oxide ($FeVO_4$, JCPDS reference card #00-030-0667) phases appear in the XRD patterns of some samples.

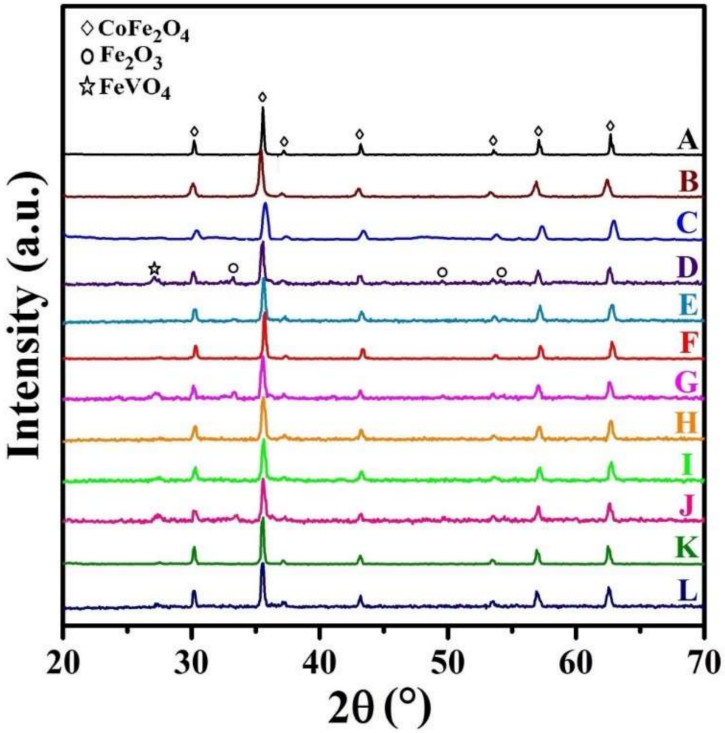

Figure 3. XRD patterns of the synthesized samples.

In our previous study [43], it was reported that the amount of the impurity/secondary phases is sharply increased by co-substitution V atoms at Co-sites, while the impurity/secondary phases of Fe_2O_3 and $FeVO_4$ are only observed in some of the XRD patterns, where V atoms occupy Fe-sites (as presented in Figure 3). Therefore, it could be concluded that vanadium atoms are easier to occupy iron positions. Thus, the substitution of vanadium for iron will induce the replacement of Fe^{3+} by V^{3+} cations, and therefore the pure spinel structure of cobalt ferrite can be observed (sample C), which is in very good agreement with the observations by Heiba et al. [45].

It is notable that the cation distribution is changed with the presence of doping elements. Consequently, the cation distribution may be changed in the doped samples. Although the vanadium ions mainly occupy the tetrahedral sites, some octahedral sites may be occupied by adding a low amount of vanadium [45], which is in good agreement with that obtained in XRD patterns of samples D, G, and J. The presence of a secondary phase in these samples can be due to this phenomenon.

The average crystalline size of cobalt ferrite nanoparticles are calculated from line width of (311) peak using Scherer's formula after taking into account the instrumental broadening [51];

$$D = \frac{0.89\lambda}{\beta \mathrm{Cos}\theta} \quad (1)$$

where 'D' is the crystallite size; 'λ' is the X-ray wavelength (1.5406 Å); 'β' is the full width at half maximum (FWHM) for (311) peak, and 'θ' is the diffraction angle [52]. The obtained results are presented in Table 3. As seen, the average crystallite size in the doped samples is smaller. However, the average crystallites size decreases initially with the doping of zinc but increases again with the doping by more significant amounts of zinc, which is in good agreement with the other observation [46]. The result specifies that the lower amount of zinc (x = 0.0, 0.1, and 0.2) delays the growth of the crystallite size; meanwhile, the larger amount of zinc favors the growth of the crystallite size at the nucleation centers, which resulted in higher crystallite size.

Table 3. Structural parameters of the synthesized samples.

Sample Code	Crystallite/Grain Size (nm)			X-ray Density (gr/cm^3)	Lattice Parameter (Å)		Volume (Å^3)
	XRD		FE-SEM		Rietveld Analysis	XRD	
	Debye-Scherrer' Formula	Rietveld Analysis					
A	45	74.3	63.9	5.32	8.39275	8.364	585.11
B	30.33	31.1	46.6	5.23	8.42654	8.409	594.61
C	32.39	34.3	-	5.41	8.38041	8.318	575.53
D	29.11	46.9	-	5.27	8.38874	8.387	590.11
E	30.98	42.4	-	5.33	8.38933	8.357	583.83
F	36.44	52.0	-	5.36	8.38883	8.345	581.06
G	23.86	43.1	-	5.32	8.39411	8.364	585.22
H	25.54	36.9	-	5.73	8.40177	8.371	586.62
I	24.67	39.1	-	5.32	8.40215	8.364	585.22
J	32.35	39.5	65.31	5.31	8.42509	8.367	585.92
K	38.31	61.0	59.3	5.29	8.42363	8.377	588.01
L	32.35	49.5	-	5.30	8.42048	8.374	587.31

In addition, the structural parameters for all synthesized samples were calculated using the Rietveld refinement method. These parameters are listed in Table 3. As seen, there is a good agreement between the results obtained by Scherer's formula and Rietveld method. However, there is a slight difference between them, which can be due to the presence of hematite impurities in some samples, because one of the hematite peaks overlaps with the (311) peak around 36°.

On the other hand, the values of the lattice constant, the unit cell volume, and the X-ray density of $Co_{1-x}Zn_xFe_{2-y}V_yO_4$ nanoparticles are determined using the equations given in Ref. [43]. These results are also presented in Table 3. As seen, the doping by Zn increases the values of the lattice constant/volume, because the Zn^{2+} ions (0.82 Å) are larger than the Co^{2+} ions (0.75 Å) [47]. Additionally, the crystallographic theoretical density values increase with an increase in zinc and vanadium content up to 0.2 and 0.15, respectively. The crystallographic density is dependent on the molecular weight of atoms and the lattice constant, which can be affected by doping.

As presented in Table 3, the lattice parameter is decreased by an increase in the vanadium value. This could be correlated with the variation of the cation distribution. On the other hand, the addition of zinc and vanadium ions can be changed the cation distribution out of the ideal state, so cobalt cations have more opportunity to occupy

the tetrahedral sites. Hence, Fe^{3+} ions located in the tetrahedral sites are forced to leave their location and shift to the octahedral sites. However, according to the ionic radius arrangement of these elements (V^{5+} (0.36 Å) < Fe^{3+} (0.64 Å) < Co^{2+} (0.75 Å) < Zn^{2+} (0.82 Å)), with the substitution of zinc instead of cobalt, it is expected to increase the lattice parameter. Furthermore, substitution of elements will cause the structure strain and prevent the growth of crystallites.

3.3. Microstructural Observations

Figure 4 shows the morphologies along with particle size distribution in the synthesized nanoparticles for samples A, B, J, and K. Additionally, the average grain size for these samples, extracted from FE-SEM images, is listed in Table 3.

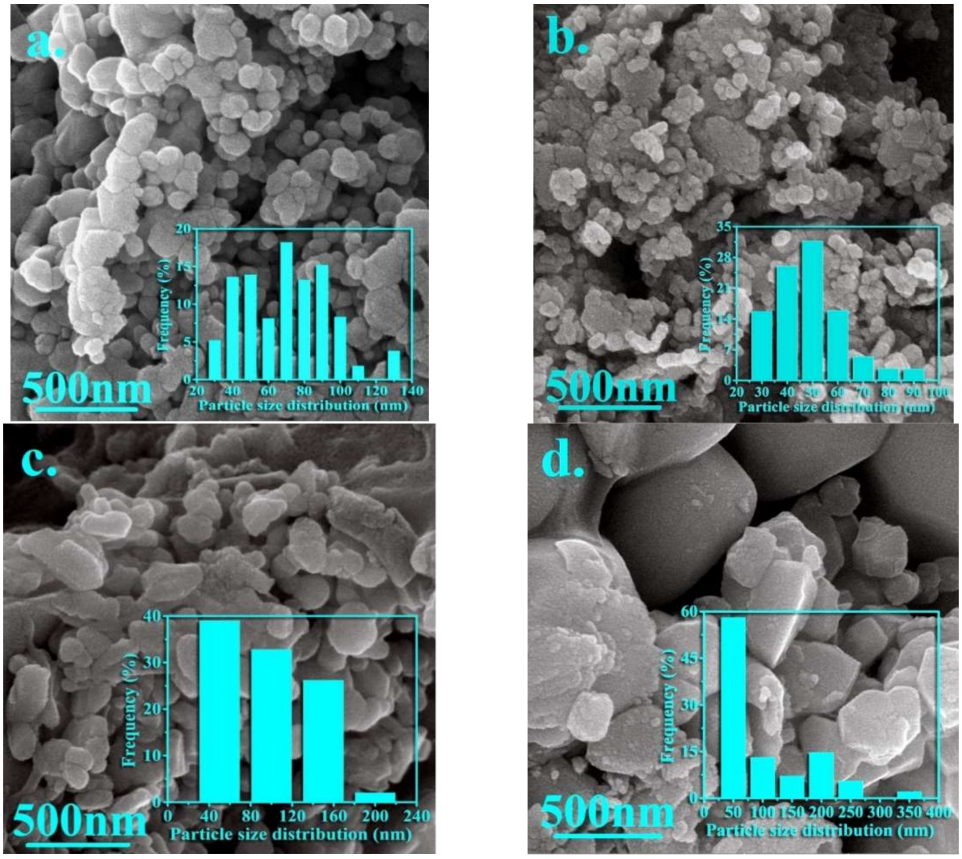

Figure 4. FE-SEM images of the nanoparticles synthesized in the samples (**a**) A, (**b**) B, (**c**) J, and (**d**) K.

It is notable that an inhomogeneous strain distribution can be created due to the difference in ionic radii of the cations, so that inhomogeneous strain distribution can form the particles with a random size and irregular shape. As seen in Figure 4a, the uniform nanoparticles with refined grains, spherical shapes, and some agglomeration can be observed for sample A. Figure 4b shows the spherical and flaky shape for the nanoparticles synthesized in sample B. Additionally, it can be seen that agglomeration is increased by adding zinc, but the average grain size is decreased from 63 to 46 nm. However, two types of particles with different morphologies can be observed by simultaneously adding zinc and vanadium, so that larger particles can be related to the presence of impurity particles (hematite and iron vanadium oxide). However, it can be seen that the agglomeration is severely reduced by simultaneously adding elements.

The optimal ratio of both elements results in a homogeneous distribution of particles. As observed in these pictures, the particles are mostly spherical or semi-spherical. However, it is notable that the agglomeration of nanoparticles can be due to the interactions of the

magnetic surface of nanoparticles. Thus, the morphology, uniformity, and agglomeration of synthesized nanoparticles can be changed in the presence of doping elements (please see Figure 4c,d).

It is notable that the average crystallite/particle sizes calculated by XRD and FE-SEM respectively are different from each other, which can be due to the formation of every particle by aggregation of a large number of crystallites or grains and also strain over the surface of the nanoparticles can cause on the further broadening of XRD peak profiles.

3.4. FTIR

FTIR Spectroscopy is a very useful tool to investigate the vibrational properties of molecules in the synthesized samples. For instance, the FTIR spectra related to the nanoparticles synthesized in the samples A, F, and K are presented in Figure 5. The results indicate that products of all three samples A, F, and K have the same molecular structure. As seen, two main absorption bands (M-O) at 489 cm^{-1} and 593 cm^{-1} are observed, which are the characteristic of spinel ferrite [53]. The first and the second bands of absorption are related to intrinsic lattice vibrations of the octahedral (v_1) and tetrahedral (v_2) sites. The difference in vibrational frequencies is due to the long bond length of oxygen-metal ions in the tetrahedral positions, which is dependent upon the bonding force, cation mass, and oxygen-metal distance [54,55]. In addition, it is observed that co-substitution of Zn and V ions causes at first a slightly shift of band positions toward the high wave number and then to the low wavenumber. As mentioned, it can be due to the change in the crystalline size of nanoparticles and also the cation distribution between the tetrahedral and octahedral sites. The higher wavenumber shows the vibration of Fe^{3+}–O^{2-} at tetrahedral sites and the lower wavenumber depicts the trivalent metal-oxygen vibration at octahedral sites.

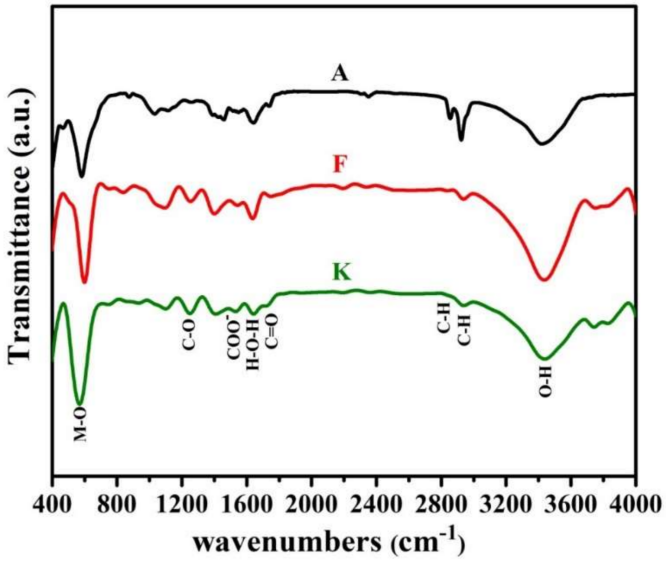

Figure 5. FT-IR spectra for the synthesized samples A, F, and K.

In addition, other peaks are marked, and sufficient description of them has been provided in previous articles [17,56].

3.5. Magnetic Properties

The hysteresis loops (*M*–*H*) of $Co_{1-x}Zn_xFe_{2-y}V_yO_4$ nanoparticle with (x = 0.0, 0.1, 0.2, 0.5 and y = 0.00, 0.05, 0.15, 0.25) were laid out in Figure 6. These magnetic measurements provide information about magnetic parameters such as saturation magnetization (M_s), coercivity (H_c), remanent magnetization (M_r), magnetic anisotropy (K), magnetic moment (n_B in Bohr magneton), and squareness ratio (M_r/M_s) ratio that is listed in Table 4. It is

necessary to mention that the values of K, n_B, and M_r/M_s ratio were calculated by the equations presented in previous articles [43,47].

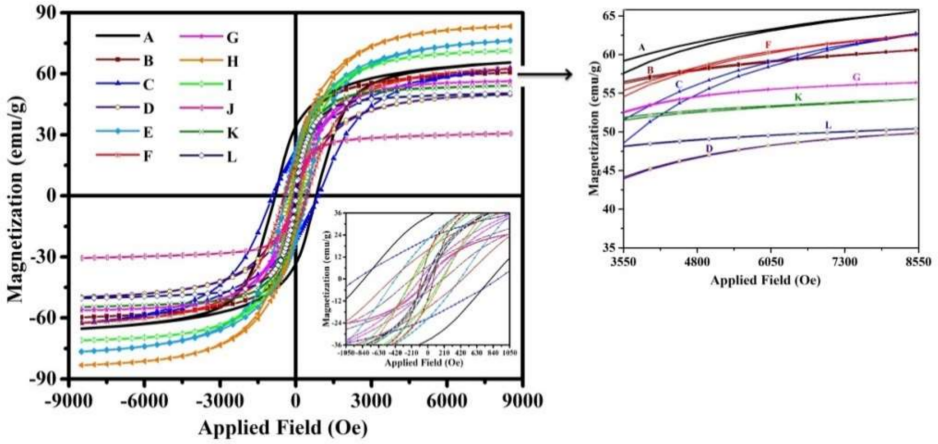

Figure 6. M-H loops of all synthesized nanoparticles at room temperature.

Table 4. Magnetic properties of the synthesized nanoparticles.

Sample Code	M_s (emu/g)	H_c (Oe)	M_r (emu/g)	$K \times 10^4$ (erg/g)	n_B	M_r/M_s
A	65.6	820.3	33.9	5.50	2.75	0.51
B	60.7	84.4	13	5.22	2.54	0.21
C	62.7	913.6	21.8	5.84	2.63	0.34
D	49.8	204.9	6.8	1.04	2.09	0.13
E	76.4	415.9	21.7	3.24	3.20	0.28
F	62.6	458	15.8	2.92	2.62	0.25
G	56.3	96.8	5	0.55	2.36	0.08
H	83.1	202.6	15	1.71	3.49	0.18
I	71.2	184.3	12.8	1.33	2.99	0.17
J	30.5	15.7	0.94	0.04	1.28	0.03
K	54.3	35.8	3.5	0.19	2.28	0.06
L	50.7	27.2	2.9	0.14	2.12	0.05

For better comparison, the values of M_s, M_r, and H_c versus dopants contents are shown in Figure 7a–c, respectively.

As presented, sample H represented the highest M_s, (Figure 7a) so that the saturation magnetization in this sample is ~27% higher than in sample A, which indicates that adding intermediate amounts of doping elements can have the more significant effect on this magnetic property. It can be explained based on cation distribution and the exchange interactions between A and B sites. Additionally, it is reported that this magnetic property can be increased with increasing vanadium content due to spin canting and disorder in the surface spin [57]. Of course, the effect of the presence of impurity phases on the saturation magnetization of the samples is also noticeable, so that, as expected, the presence of impurity phases reduces this property.

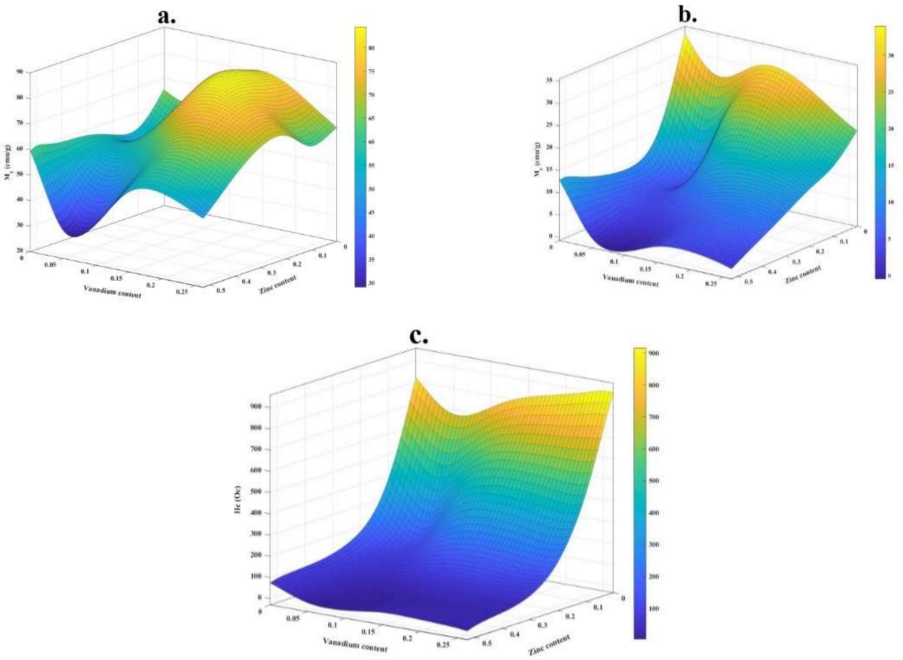

Figure 7. Variation of (**a**) M_S, (**b**) M_r, and (**c**) H_c as a function of Zn and V contents.

On the other hand, it is shown that the addition of Zn decreases M_r in the synthesized nanoparticles (Figure 7b), so that the minimum of M_r is observed for sample J (~0.94 emu/g). It is also well observed that sample J has the lowest amount of coercivity, which is in good agreement with that reported in the literature [47,58]. However, adding vanadium prevents this reduction.

The highest value of coercivity is obtained for sample C, which is equal to ~913 Oe (Table 4). Figure 7c shows that with the addition of vanadium, this magnetic parameter increases, while with the addition of zinc, it decreases. This magnetic parameter is affected by the presence of impurity phases and various structural defects, i.e., dislocations, grain boundaries, anisotropy, and precipitates.

As seen in Table 4, the amount of M_r has a good relationship with the amount of K in which with adding zinc, the value of K decreases to ~0.04 erg/g. The maximum value of K is obtained for sample A, which can be due to the presence of Co^{2+} ions in octahedral sites. Furthermore, with the co-substitution of zinc and vanadium, the presence of cobalt ions in octahedral sites is reduced due to the changes in cation distribution.

Finally, it can be concluded that the magnetic behavior of the samples can be affected by three important factors; (i) the presence of secondary/impurity phases, (ii) cation distribution in the spinel structure, and (iii) the size of the crystallites/grains.

4. Conclusions

The effect of zinc and vanadium doping on the microstructure, and structural and magnetic properties of cobalt ferrite synthesized by modified sol-gel method was investigated. The formation of cubic spinel structure is confirmed by XRD. The cation distribution also showed that V^{5+} tended to be located in tetrahedral sites. Nevertheless, by adding a low concentration of these elements, it can also occupy octahedral sites. Hence, the formation of a secondary/impurity phase such as hematite and vanadium iron oxide in these conditions is inevitable. The ionic radius arrangement of these elements (V^{5+} (0.36 Å) < Fe^{3+} (0.64 Å) < Co^{2+} (0.75 Å) < Zn^{2+} (0.82 Å)), it makes sense to create and increase stress and strain in the spinel lattice, which can inhibit the growth of crystals. FTIR spectra revealed the absorption peaks near 489 and 593 cm^{-1} that affirms the ferrite behavior of the samples. The FE-SEM micrographs revealed some fine-sized agglomerated semi-spherical-shaped particles. The agglomerated grains indicated the strong interactions

between the particles and continuity of the grain growth during sintering. The hysteresis curves showed that the increase and decrease in magnetic properties could be due to the replacement cations.

Author Contributions: Conceptualization, S.H. and A.S.; Formal analysis, S.H. and M.N.; Investigation, P.I.; Methodology, S.H. and A.S.; Project administration, M.N.; Software, P.I.; Supervision, S.H., A.S. and M.N.; Visualization, P.I.; Writing—original draft, S.H.; Writing—review & editing, S.H. and A.S. All authors have read and agreed to the published version of the manuscript.

Funding: This research received no external funding.

Conflicts of Interest: The authors declare no conflict of interest.

References

1. Mathubala, G.; Manikandan, A.; Antony, S.A.; Ramar, P. Photocatalytic degradation of methylene blue dye and magneto- optical studies of magnetically recyclable spinel $Ni_xMn_{1-x}Fe_2O_4$ (x = 0.0–1.0) nanoparticles. *Nanoparticles* **2016**, *1113*, 79–87. [CrossRef]
2. El-Ghazzawy, E. Effect of heat treatment on structural, magnetic, elastic and optical properties of the co-precipitated $Co_{0.4}Sr_{0.6}Fe_2O_4$. *J. Magn. Magn. Mater.* **2019**, *497*, 166017. [CrossRef]
3. Hema, E.; Manikandan, A.; Karthika, P.; Arul, S.; Venkatraman, B.R. A Novel Synthesis of Zn^{2+} -Doped $CoFe_2O_4$ *Spinel* Nanoparticles: Structural, Morphological, Opto-magnetic and Catalytic Properties. *J. Supercond. Nov. Magn.* **2015**, *28*, 2539–2552. [CrossRef]
4. Javaid, R.; Nanba, T. $MgFe_2O_4$-Supported Ru Catalyst for Ammonia Synthesis: Promotive Effect of Chlorine. *ChemistrySelect* **2020**, *5*, 4312–4315. [CrossRef]
5. Abasum, A.; Alghuthaymi, M.; Qazi, U.Y.; Shahid, I.; Abbas, Q.; Javaid, R.; Nadeem, N.; Zahid, M. UV-Accelerated Photocatalytic Degradation of Pesticide over Magnetite and Cobalt Ferrite Decorated Graphene Oxide Composite. *Plants* **2020**, *10*, 6. [CrossRef]
6. Ramakrishna, A.; Murali, N.; Mammo, T.W.; Samatha, K.; Veeraiah, V. Structural and DC electrical resistivity, magnetic properties of $Co_{0.5}M_{0.5}Fe_2O_4$ (M=Ni, Zn, and Mg) ferrite nanoparticles. *Phys. B Condens. Matter* **2018**, *534*, 134–140. [CrossRef]
7. Staruch, M.; Hires, D.; Violette, D.; Navarathne, D.; Sotzing, G.A.; Jain, M. Structural and magnetic properties of CoFe2O4and Co0.5Zn0.5Fe2O4nanoparticles for the magnetoelectric composite films. *Integr. Ferroelectr.* **2011**, *131*, 102–109. [CrossRef]
8. Ansari, S.; Sinha, B.B.; Pai, K.R.; Bhat, S.K.; Ma, Y.-R.; Sen, D.; Kolekar, Y.D.; Ramana, C. Controlled surface/interface structure and spin enabled superior properties and biocompatibility of cobalt ferrite nanoparticles. *Appl. Surf. Sci.* **2018**, *459*, 788–801. [CrossRef]
9. Sanpo, N.; Tharajak, J.; Li, Y.; Berndt, C.; Wen, C.; Wang, J. Biocompatibility of transition metal-substituted cobalt ferrite nanoparticles. *J. Nanopart. Res.* **2014**, *16*, 2510. [CrossRef]
10. Habib, A.H.; Ondeck, C.L.; Chaudhary, P.; Bockstaller, M.R.; McHenry, M.E. Evaluation of iron-cobalt/ferrite core-shell nanoparticles for cancer thermotherapy. *J. Appl. Phys.* **2008**, *103*, 7–9. [CrossRef]
11. Ahmad, S.I.; Rauf, A.; Mohammed, T.; Bahafi, A.; Kumar, D.R.; Suresh, M.B. Dielectric, impedance, AC conductivity and low-temperature magnetic studies of Ce and Sm co-substituted nanocrystalline cobalt ferrite. *J. Magn. Magn. Mater.* **2019**, *492*, 165666. [CrossRef]
12. Haïk Dunn, I.; Jacobo, S.E.; Bercoff, P.G. Structural and magnetic influence of yttrium-for-iron substitution in cobalt ferrite. *J. Alloys Compd.* **2017**, *691*, 130–137. [CrossRef]
13. Vaithyanathan, V.; Ugendar, K.; Chelvane, J.A.; Bharathi, K.K.; Inbanathan, S. Structural and magnetic properties of Sn and Ti doped Co ferrite. *J. Magn. Magn. Mater.* **2015**, *382*, 88–92. [CrossRef]
14. Amiri, S.; Shokrollahi, H. The role of cobalt ferrite magnetic nanoparticles in medical science. *Mater. Sci. Eng. C* **2013**, *33*, 1–8. [CrossRef] [PubMed]
15. Afshari, M.; Isfahani, A.-R.R.; Hasani, S.; Davar, F.; Ardakani, K.J. Effect of apple cider vinegar agent on the microstructure, phase evolution, and magnetic properties of CoFe2O4magnetic nanoparticles. *Int. J. Appl. Ceram. Technol.* **2019**, *16*, 1612–1621. [CrossRef]
16. Joshi, S.; Kumar, M.; Chhoker, S.; Kumar, A.; Singh, M. Effect of Gd3+substitution on structural, magnetic, dielectric and optical properties of nanocrystalline $CoFe_2O$. *J. Magn. Magn. Mater.* **2017**, *426*, 252–263. [CrossRef]
17. Hashemi, S.M.; Hasani, S.; Ardakani, K.J.; Davar, F. The effect of simultaneous addition of ethylene glycol and agarose on the structural and magnetic properties of $CoFe_2O_4$ nanoparticles prepared by the sol-gel auto-combustion method. *J. Magn. Magn. Mater.* **2019**, *492*, 165714. [CrossRef]
18. Ghosh, M.P. Microstructural, magnetic, and hyperfine characterizations of Cu—Doped cobalt ferrite nanoparticles. *J. Am. Ceram. Soc.* **2019**, *102*, 7509–7520. [CrossRef]
19. Meng, X.; Li, H.; Chen, J.; Mei, L.; Wang, K.; Li, X. Mössbauer study of cobalt ferrite nanocrystals substituted with Mo rare-earth Y^{3+} ions. *J. Magn. Magn. Mater.* **2009**, *321*, 1155–1158. [CrossRef]
20. Patankar, K.K.; Ghone, D.M.; Mathe, V.L.; Kaushik, S.D. Structural and physical property study of sol–gel synthesized $CoFe_2-xHoxO_4$nano ferrites. *J. Magn. Magn. Mater.* **2018**, *454*, 71–77. [CrossRef]

21. Dippong, T.; Cadar, O.; Levei, E.A.; Deac, I.G.; Diamandescu, L.; Barbu-Tudoran, L. Influence of cobalt ferrite content on the structure and magnetic properties of $(CoFe_2O_4)X$ $(SiO_2\text{-}PVA)_{100\text{-}X}$ nanocomposites. *Ceram. Int.* **2018**, *44*, 7891–7901. [CrossRef]
22. Gul, I.H.; Maqsood, A. Structural, magnetic and electrical properties of cobalt ferrites prepared by the sol–gel route. *J. Alloys Compd.* **2008**, *465*, 227–231. [CrossRef]
23. Mohamed, R.; Rashad, M.; Haraz, F.; Sigmund, W. Structure and magnetic properties of nanocrystalline cobalt ferrite powders synthesized using organic acid precursor method. *J. Magn. Magn. Mater.* **2010**, *322*, 2058–2064. [CrossRef]
24. Sanchez-Marcos, J.; Mazario, E.; Rodriguez-Velamazan, J.; Salas, E.; Herrasti, P.; Menendez, N. Cation distribution of cobalt ferrite electrosynthesized nanoparticles. A methodological comparison. *J. Alloys Compd.* **2018**, *739*, 909–917. [CrossRef]
25. Karimi, Z.; Mohammadifar, Y.; Shokrollahi, H.; Asl, S.K.; Yousefi, G.; Karimi, L. Magnetic and structural properties of nano sized Dy-doped cobalt ferrite synthesized by co-precipitation. *J. Magn. Magn. Mater.* **2014**, *361*, 150–156. [CrossRef]
26. Javaid, R.; Nanba, T. Effect of preparation method and reaction parameters on catalytic activity for ammonia synthesis. *Int. J. Hydrogen Energy* **2021**, *46*, 35209–35218. [CrossRef]
27. Jnaneshwara, D.; Avadhani, D.; Prasad, B.D.; Nagabhushana, B.; Nagabhushana, H.; Sharma, S.; Prashantha, S.; Shivakumara, C. Effect of zinc substitution on the nanocobalt ferrite powders for nanoelectronic devices. *J. Alloys Compd.* **2014**, *587*, 50–58. [CrossRef]
28. Yonatan Mulushoa, S.; Murali, N.; Tulu Wegayehu, M.; Margarette, S.J.; Samatha, K. Influence of Cu-Cr substitution on structural, morphological, electrical and magnetic properties of magnesium ferrite. *Results Phys.* **2018**, *8*, 772–779. [CrossRef]
29. Gheisari, K.; Javadpour, S.; Shokrollahi, H.; Hashemi, B. Magnetic losses of the soft magnetic composites consisting of iron and Ni–Zn ferrite. *J. Magn. Magn. Mater.* **2008**, *320*, 1544–1548. [CrossRef]
30. Yadav, R.S.; Havlica, J.; Kuřitka, I.; Kozakova, Z.; Palou, M.; Bartoníčková, E.; Boháč, M.; Frajkorová, F.; Masilko, J.; Kalina, L.; et al. Magnetic Properties of Dysprosium-Doped Cobalt Ferrite Nanoparticles Synthesized by Starch-Assisted Sol-Gel Auto-combustion Method. *J. Supercond. Nov. Magn.* **2015**, *28*, 2097–2107. [CrossRef]
31. Rouhani, A.R.; Esmaeil-Khanian, A.H.; Davar, F.; Hasani, S. The effect of agarose content on the morphology, phase evolution, and magnetic properties of $CoFe_2O_4$ nanoparticles prepared by sol-gel autocombustion method. *Int. J. Appl. Ceram. Technol.* **2017**, *15*, 758. [CrossRef]
32. Sakka, S.; Petrykin, V.; Kakihana, M. *Sol-Gel Science and Technology. Sol-Gel Processing*; Springer Science & Business Media: Berlin/Heidelberg, Germany, 2005; p. 680.
33. Sanpo, N.; Wang, J.; Berndt, C.C. Sol-Gel Synthesized Copper-Substituted Cobalt Ferrite Nanoparticles for Biomedical Applications. *J. Nano Res.* **2013**, *22*, 95–106. [CrossRef]
34. Davar, F.; Shayan, N.; Hojjati-Najafabadi, A.; Sabaghi, V.; Hasani, S. Development of ZrO_2-MgO nanocomposite powders by the modified sol-gel method. *Int. J. Appl. Ceram. Technol.* **2017**, *14*, 211–219. [CrossRef]
35. Amiri, M.; Salavati-Niasari, M.; Akbari, A. Magnetic nanocarriers: Evolution of spinel ferrites for medical applications. *Adv. Colloid Interface Sci.* **2019**, *265*, 29–44. [CrossRef] [PubMed]
36. Topkaya, R.; Kurtan, U.; Junejo, Y.; Baykal, A. Sol–gel auto combustion synthesis of $CoFe_2O_4$/1-methyl-2-pyrrolidone nanocomposite with ethylene glycol: Its magnetic characterization. *Mater. Res. Bull.* **2013**, *48*, 3247–3253. [CrossRef]
37. Rani, B.J.; Ravina, M.; Saravanakumar, B.; Ravi, G.; Ganesh, V.; Ravichandran, S.; Yuvakkumar, R. Ferrimagnetism in cobalt ferrite ($CoFe_2O_4$) nanoparticles. *Nano-Struct. Nano-Objects* **2018**, *14*, 84–91. [CrossRef]
38. Tatarchuk, T.; Paliychuk, N.; Bououdina, M.; Al-Najar, B.; Pacia, M.; Macyk, W.; Shyichuk, A. Effect of cobalt substitution on structural, elastic, magnetic and optical properties of zinc ferrite nanoparticles. *J. Alloys Compd.* **2018**, *731*, 1256–1266. [CrossRef]
39. Kokare, M.; Jadhav, N.A.; Kumar, Y.; Jadhav, K.M.; Rathod, S. Effect of Nd^{3+} doping on structural and magnetic properties of $Ni_{0.5}Co_{0.5}Fe_2O_4$ nanocrystalline ferrites synthesized by sol-gel auto combustion method. *J. Alloys Compd.* **2018**, *748*, 1053–1061. [CrossRef]
40. Lima, A.; Peres, A.; Araújo, J.; Morales, M.; Medeiros, S.; Soares, J.S.; Melo, D.; Carriço, A. The effect of Sr^{2+} on the structure and magnetic properties of nanocrystalline cobalt ferrite. *Mater. Lett.* **2015**, *145*, 56–58. [CrossRef]
41. Kumar, L.; Kumar, P.; Kar, M. Cation distribution by Rietveld technique and magnetocrystalline anisotropy of Zn substituted nanocrystalline cobalt ferrite. *J. Alloys Compd.* **2013**, *551*, 72–81. [CrossRef]
42. Dippong, T.; Goga, F.; Levei, E.-A.; Cadar, O. Influence of zinc substitution with cobalt on thermal behaviour, structure and morphology of zinc ferrite embedded in silica matrix. *J. Solid State Chem.* **2019**, *275*, 159–166. [CrossRef]
43. Imanipour, P.; Hasani, S.; Seifoddini, A.; Farnia, A.; Karimabadi, F.; Jahanbani-Ardakani, K.; Davar, F. The possibility of vanadium substitution on Co lattice sites in CoFe2O4 synthesized by sol-gel autocombustion method. *J. Sol-Gel Sci. Technol.* **2020**, *95*, 157–167. [CrossRef]
44. Nakagomi, F.; de Souza, P.E.N.; Castro, T.; Garg, V.; Oliveira, A.; e Silva, F.; Franco, A.; Morais, P.; da Silva, S.W. Cation distribution of Zn Co_1-Fe_2O_4 nanoparticles: A resonant X-ray diffraction study. *J. Alloys Compd.* **2020**, *842*, 155751. [CrossRef]
45. Heiba, Z.K.; Mohamed, M.B.; Ahmed, S. Cation distribution correlated with magnetic properties of cobalt ferrite nanoparticles defective by vanadium doping. *J. Magn. Magn. Mater.* **2017**, *441*, 409–416. [CrossRef]
46. Singhal, S.; Namgyal, T.; Bansal, S.; Chandra, K. Effect of Zn Substitution on the Magnetic Properties of Cobalt Ferrite Nano Particles Prepared Via Sol-Gel Route. *J. Electromagn. Anal. Appl.* **2010**, *2*, 376–381. [CrossRef]

47. Imanipour, P.; Hasani, S.; Afshari, M.; Sheykh, S.; Seifoddini, A.; Jahanbani-Ardakani, K. The effect of divalent ions of zinc and strontium substitution on the structural and magnetic properties on the cobalt site in cobalt ferrite. *J. Magn. Magn. Mater.* **2020**, *510*, 166941. [CrossRef]
48. Zare, S.; Ati, A.A.; Dabagh, S.; Rosnan, R.; Othaman, Z. Synthesis, structural and magnetic behavior studies of Zn–Al substituted cobalt ferrite nanoparticles. *J. Mol. Struct.* **2015**, *1089*, 25–31. [CrossRef]
49. Mustafa, G.; Islam, M.U.; Zhang, W.; Arshad, M.I.; Jamil, Y.; Anwar, H.; Murtaza, G.; Hussain, M.; Ahmad, M. Investigation of the Role of Ce^{3+} Substituted Ions on Dielectric Properties of Co-Cr Ferrites Prepared by Co-precipitation Method. *J. Electron. Mater.* **2016**, *45*, 5830–5838. [CrossRef]
50. Mustafa, G.; Islam, M.U.; Zhang, W.; Anwar, A.W.; Jamil, Y.; Murtaza, G.; Ali, I.; Hussain, M.; Ali, A.; Ahmad, M. Influence of the divalent and trivalent ions substitution on the structural and magnetic properties of $Mg_{0.5-x}Cd_xCo_{0.5}Cr_{0.04}Tb_yFe_{1.96-y}O_4$ ferrites prepared by sol–gel method. *J. Magn. Magn. Mater.* **2015**, *387*, 147–154. [CrossRef]
51. Cullity, B.D. *Elements of X-ray Diffraction*, 2nd ed.; Addison-Wesley Publishing Co.: New York, NY, USA, 1978.
52. Scherrer, P. Determination of size and inner structure of colloidal particles by X-ray (Bestimmung der Grösse und der inneren Struktur von Kolloidteilchen mittels Röntgenstrahlen). Nachrichten von der Gesellschaft der Wissenschaften zu Göttingen. *Math Klasse* **1918**, *1918*, 98–100.
53. Dippong, T.; Levei, E.A.; Deac, I.G.; Neag, E.; Cadar, O. Influence of Cu^{2+}, Ni^{2+}, and Zn^{2+} Ions Doping on the Structure, Morphology, and Magnetic Properties of Co-Ferrite Embedded in SiO_2 Matrix Obtained by an Innovative Sol-Gel Route. *Nanomaterials* **2020**, *10*, 580. [CrossRef] [PubMed]
54. Anugraha, A.; Lakshmi, V.K.; Kumar, G.S.; Raguram, T.; Rajni, K.S. Synthesis and Characterisation of Copper Substituted Cobalt Ferrite Nanoparticles by Sol-Gel Auto Combustion Route. In *IOP Conference Series: Materials Science and Engineering, Proceedings of the International Conference on Advances in Materials and Manufacturing Applications (IConAMMA-2018), Bengaluru, India, 16–18 August 2018*; IOP Publishing: Bristol, UK, 2019; Volume 577.
55. Jesus Mercy, S.; Murali, N.; Ramakrishna, A.; Ramakrishna, Y.; Veeraiah, V.; Samatha, K. Microstructural, thermal, electrical and magnetic analysis of Mg2+ substituted Cobalt ferrite. *Appl. Phys. A Mater. Sci. Process* **2020**, *126*, 873. [CrossRef]
56. Shayestefar, M.; Mashreghi, A.; Hasani, S.; Rezvan, M.T. Optimization of the structural and magnetic properties of $MnFe_2O_4$ doped by Zn and Dy using Taguchi method. *J. Magn. Magn. Mater.* **2021**, *541*, 168390. [CrossRef]
57. Khodair, Z.T.; Mohammad, A.M.; Khadom, A.A. Investigations of structural and magnetic properties of $Cu_{1-x}V_xO$ nanostructures prepared by sol-gel method. *Chem. Data Collect.* **2019**, *25*, 100315. [CrossRef]
58. Jadhav, S.S.; Shirsath, S.E.; Patange, S.M.; Jadhav, K.M. Effect of Zn substitution on magnetic properties of nanocrystalline cobalt ferrite. *J. Appl. Phys.* **2010**, *108*, 093920. [CrossRef]